Bulletin of the Seismological Society of America, Vol. 105, No. 2a, pp. –, April 2015, doi: 10.1785/0120130108

Fault-Slip Distribution of the 1999 M_w 7.1 Hector Mine Earthquake, California, Estimated from Postearthquake Airborne LiDAR Data

by T. Chen, S. O. Akciz, K. W. Hudnut, D. Z. Zhang, and J. M. Stock

Abstract The 16 October 1999 Hector Mine earthquake (M_w 7.1) was the first large earthquake for which postearthquake airborne Light Detection and Ranging (LiDAR) data were collected to image the fault surface rupture. In this work, we present measurements of both vertical and horizontal slip along the entire surface rupture of this earthquake based on airborne LiDAR data acquired in April 2000. We examine the details of the along-fault slip distribution of this earthquake based on 255 horizontal and 85 vertical displacements using a 0.5 m digital elevation model derived from the LiDAR imagery. The slip measurements based on the LiDAR dataset are highest in the epicentral region, and taper in both directions, consistent with earlier findings by other works. The maximum dextral displacement measured from LiDAR imagery is 6.60 ± 1.10 m, located about 700 m south of the highest field measurement (5.25 ± 0.85 m). Our results also illustrate the difficulty in resolving displacements smaller than 1 m using LiDAR imagery alone. We analyze slip variation to see if it is affected by rock type and whether variations are statistically significant. This study demonstrates that a postearthquake airborne LiDAR survey can produce an along-fault horizontal and vertical offset distribution plot of a quality comparable to a reconnaissance field survey. Although LiDAR data can provide a higher sampling density and enable rapid data analysis for documenting slip distributions, we find that, relative to field methods, it has a limited ability to resolve slip that is distributed over several fault strands across a zone. We recommend a combined approach that merges field observation with LiDAR analysis, so that the best attributes of both quantitative topographic and geological insight are utilized in concert to make best estimates of offsets and their uncertainties.

Online Material: Tables of LiDAR displacement measurements; slip distributions plots; Google Earth index files and locations where displacements were made; LiDAR data files, and access information to view screen captures of the displacement measurements.

Introduction

Measurements of surface displacements associated with large surface-rupturing earthquakes are an important foundation for improving our understanding of earthquake mechanics, dynamics of the earthquake rupture, ground motions, and estimates of seismic hazard. Such datasets from past earthquakes have been commonly used to establish and refine fault scaling relationships (e.g., Wells and Coppersmith, 1994) and characterize the geometry and slip distribution of earthquake surface ruptures (e.g., Wesnousky, 2008). Different data sources and analysis methods have been used, depending on what technology was available at the time of the study. Over the past few decades, many field mapping, geodetic, and optical-imagery-based studies have characterized surface deformation immediately after an earthquake (e.g., Landers, Hector Mine, İzmit, Denali, Wenchuan, El Mayor–Cucapah). However, the documentation of displacements associated with early historical or prehistoric earthquakes is not as straightforward. Erosion and sedimentation limit rupture mapping and the number of displacement measurements that can be reliably made. When available, aerial photos and satellite optical images complement field investigations and aid in estimating ground displacements associated with modern or past earthquakes.

Within the past decade, airborne Light Detection and Ranging (LiDAR) has provided high-resolution, 3D, digital topographic data along active faults. Hudnut, Borsa, *et al.* (2002) demonstrated that coseismic fault slip may be measured using only postearthquake LiDAR, and they initially presented

the Hector Mine dataset we examine in the current study. In other studies, airborne LiDAR has helped to identify and characterize active faults in heavily vegetated areas (Haugerud *et al.*, 2003; Prentice *et al.*, 2003; Cunningham *et al.*, 2006) and provided an opportunity to assess fault offset and slip-rate estimates based on tectonically displaced surface features along those scanned faults (e.g., Frankel and Dolan, 2007; Zielke *et al.*, 2010; Salisbury *et al.*, 2012). Postearthquake LiDAR data were used after the Wenchuan (Li, 2009), Haiti (Prentice *et al.*, 2010), El Mayor–Cucapah (Oskin *et al.*, 2012), and Darfield (Quigley *et al.*, 2012) earthquakes to complement field investigations. To date, however, no systematic along-whole-surface slip measurements based on postearthquake LiDAR data alone have been conducted with the intent of characterizing and describing data and technique limitations with respect to other methods, as we do in the present study.

The M_w 7.1 Hector Mine earthquake (Fig. 1) of 16 October 1999 occurred in an ideal geological and geomorphic setting, in which the suitability of postearthquake topographic data for accurate determination of the slip distribution may be uniquely examined. (1) Many ruptures occurred with oblique slip on a low-relief topography with minimal vegetation cover. This enabled easier identification of the fault traces and geomorphologic features that are used as reference lines or surfaces, especially in determining the vertical component of the displacement. (2) Surface rupture occurred in an area covered by relatively young deposits (Treiman *et al.*, 2002), which had not been disrupted by earthquakes for at least 10,000 years before this earthquake (Hart, 1987). All measured displacements are thus attributed with high confidence to offset during (or after) the Hector Mine earthquake. (3) Mapping surface ruptures and measuring displacements using remote sensing data, especially in rugged and hard to reach areas, constituted an efficient alternative and supplement to field observations (e.g., Haeussler *et al.*, 2004; Binet and Bollinger, 2005; Klinger *et al.*, 2005; Liu-Zeng *et al.*, 2009). However, in these approaches, airborne and satellite imagery are generally projected onto a 2D horizontal plane, and most of the elevation-dimension information is lost. Although this does not limit a researcher's ability to measure displacements for pure strike-slip earthquakes, it provides less complete information in earthquakes with an oblique or pure dip-slip component. In contrast, LiDAR data are capable of representing the 3D surface topography at very high resolution and quantifying 3D surface displacements. (4) The Hector Mine earthquake surface rupture crossed three main lithologies, enabling us to explore the relationship between rock type and clarity and abundance of observable offset features (compares rock type to two characteristics of offset features). The rupture crossed (a) Quaternary basaltic lava flows, (b) Pleistocene alluvial fan and playa sediments, and (c) Tertiary volcanic flows and pyroclastic deposits, interbedded with some sandstone and conglomerate (Treiman *et al.*, 2002). (5) Evaluations of along-strike surface slip variation require spatially dense surface slip data. It is not clear whether a high-resolution topographic dataset alone is capable of providing such an accurate slip distribution plot when a surface rupture occurs in an area where cultural features are not abundant or in different geological formations with differing geomorphic line formation and preservation characteristics.

In this work, we present measurement results of both vertical and horizontal slip along the entire surface rupture of the Hector Mine earthquake based on an airborne LiDAR survey conducted six months after the earthquake (Hudnut, Borsa, *et al.*, 2002). In addition to characterizing the near-field surface displacements based entirely on the LiDAR data, we also discuss the suitability of using postearthquake topographic data to quantify the coseismic slip distribution.

Geological Setting

The Hector Mine earthquake generated an approximately 45 km long surface rupture in the Mojave Desert section of the eastern California shear zone (ECSZ) (Treiman *et al.*, 2002). The ECSZ is an 80 km wide, 400 km long zone of right-lateral strike-slip shearing that accommodates as much as 12 mm/yr of the plate motion between the Pacific and North American plates (Sauber *et al.*, 1994). Surface rupture associated with the Hector Mine earthquake occurred on the Lavic Lake fault, the Bullion fault (including the western and the eastern strands), the Mesquite Lake fault, and the "A" fault from Bortugno (1987) (Fig. 1) (Treiman *et al.*, 2002).

The Lavic Lake fault can be divided into five subsections (Rymer *et al.*, 2002): the northernmost section, north of the Lavic Lake playa section, the Lavic Lake section, south of the Lavic Lake playa section, and the Bullion Mountains section. The first (northernmost) section of the Lavic Lake fault ruptured across late Quaternary basalt flows and had many millimeter-width tension fractures with local right-lateral offsets up to a few centimeters and sparse left-lateral offsets up to 1 cm (Treiman *et al.*, 2002). These are too small to see in airborne LiDAR data. In the second section, on the northern side of the Lavic Lake playa, the main surface rupture spread into a broad zone (much wider than ~50 m) within the alluvial fan area. Although most of the displacements were small (< 1 m), resolution of the digital elevation model (DEM) was enough to permit numerous horizontal and vertical offset measurements. In the third section, across the fine-grained Lavic Lake playa sediments, surface rupture became well defined in a 40 m wide zone with sequential left-stepping, echelon fractures (Ⓔ see Google Earth index files S1 and S2, available in the electronic supplement to this article). Because of a lack of clearly definable discrete features that could be correlated across the fault trace, it was difficult to measure horizontal offsets. However, because the original playa surface should have been planar before the 1999 earthquake, we were able to measure the vertical component of offset of the deformed playa surface. In the fourth section, south of the playa, gullies within the medium- to coarse-grained alluvial fan deposits provided numerous sites where offset could be measured (Ⓔ see Google Earth index files S3 and S4). The fifth (Bullion Mountains) section, where the maximum slip was measured in the field, is near the

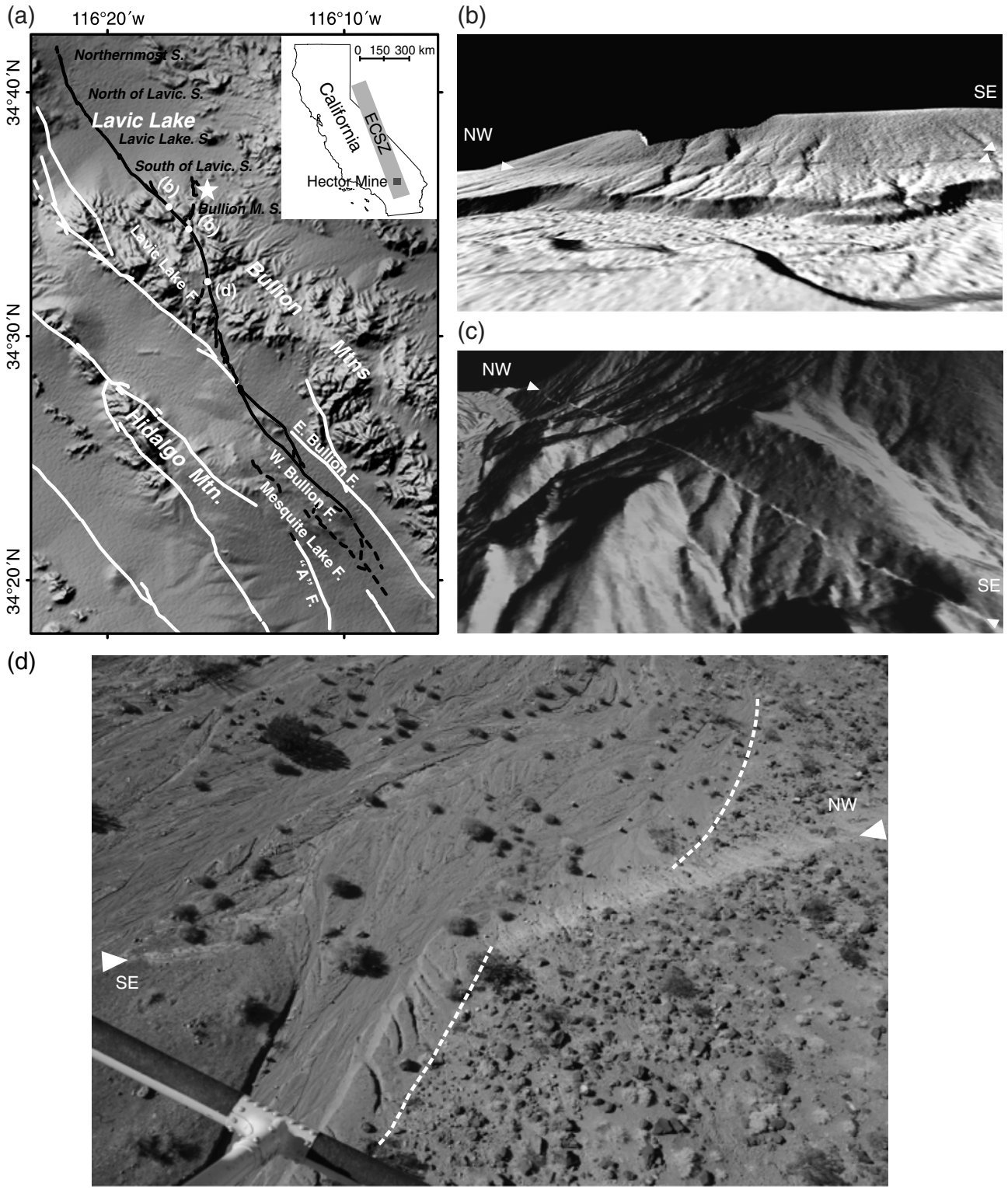

Figure 1. (a) Overview of surface rupture covered (solid black lines) or not covered (black dashed lines) by LiDAR, associated with the Hector Mine earthquake shown on a gray-scale shaded relief map derived from Shuttle Radar Topography Mission data (see Data and Resources). The epicenter of the earthquake is shown by the white star, and white lines represent the adjacent fault zone system. The inset map indicates the context of the Hector Mine rupture within the northwest-striking dextral faults of the eastern California shear zone (ECSZ, gray band on inset map of California). (b) and (c) Oblique perspective view of portions of the fault scarp in gray-scale shaded relief map. (b) The view is from southwest (SW) to northeast (NE), and the illumination is 315° with northwest–southeast azimuth. (c) The view is from southwest to northeast, and the illumination is 135° with southeast–northwest azimuth. (d) Oblique aerial photograph of the maximum LiDAR lateral offset measured from LiDAR data (site ID 167) taken from a helicopter in December 2012. The white dashed lines are used to indicate the channel slope on both sides of the fault. White solid triangles indicate the local surface rupture of the Hector Mine earthquake.

mainshock epicenter. Here, Tertiary bedrock units were ruptured, and rupture in this section extended southeastward to a complex junction between the Lavic Lake fault and the Bullion fault along the western margin of the Bullion Mountains. Along much of the primary fault, the rupture is less than 2 m wide, and the displacements are clear and abrupt. Secondary strands define a zone as much as 20 m wide along significant parts of this segment (Rymer *et al.*, 2002; Treiman *et al.*, 2002). Numerous discrete gullies and ridges could be correlated across the fault trace in this section (Ⓔ see Google Earth index files S3 and S4).

Southeast of the junction between the Lavic Lake fault and the Bullion fault system, the surface rupture splits into the West and East Bullion fault. The fault traces are clear and continuous, concentrated along each of the two strands. Slip along the East Bullion fault gradually diminishes until it finally becomes one splay of the West Bullion fault. Surface rupture on the West Bullion fault was mapped as far south as the edge of the LiDAR scanning coverage (Hudnut, Borsa, *et al.*, 2002). Near the southern end of the rupture, surface faulting became discontinuous and small magnitude displacements and the tensional component of the cracks resulted in the identification of only a few offset features in the field (Treiman *et al.*, 2002).

The Mesquite Lake fault and the "A" fault were not scanned in the LiDAR flight due to insignificant rupture and time limitations. The Hector Mine Earthquake Geologic Working Group (1999) mapped the surface-fault rupture and documented the slip distribution with about 300 measurements along the rupture (Treiman *et al.*, 2002). In this article, we independently estimated 255 horizontal and 85 vertical displacements, concentrating on the Lavic Lake fault and the Bullion fault, covering ~90% of the whole rupture.

LiDAR Data Acquisition

Six months after the Hector Mine earthquake, an investigation team funded by the U.S. Geological Survey and Southern California Earthquake Center facilitated the scan of the main surface rupture and its surrounding region (Hudnut, Borsa, *et al.*, 2002). Using a helicopter-mounted scanner, a swath width of ~125 m on average, along ~70 km of flight lines, was obtained in a single day, covering all of the main fault breaks known at that time (48 km; Treiman *et al.*, 2002), as well as unruptured sections of the Bullion fault. An onboard Global Positioning System (GPS) and an integrated inertial-navigation system allowed precise positioning of the platform. Over 70 million data points were collected with GPS ground control provided by the nearby continuously operating ground GPS stations (Hudnut, Borsa, *et al.*, 2002). This was the first time that the entire length along the surface rupture was documented with a scanning laser swath mapping system soon after a ground-rupturing earthquake.

The system scan rate was 6888 pulses per second, and the aircraft was flown lower and slower than was typically done at that time using fixed-wing aircraft and scanners (Hudnut, Borsa, *et al.*, 2002). Consequently, the shot point density of the April 2000 LiDAR is typically around 5 or 6 points per square meter. This data density was sufficient for us to produce 0.5 m DEMs along the entire swath. Ⓔ The point cloud files and hillshade Google Earth index files that were produced during this study are available in the electronic supplement. All file contents are from the original work of Hudnut, Borsa, *et al.* (2002) but are now being made available with different file formats.

Methodology

Raw Data Preparation

Following data acquisition in 2000, LiDAR data were stored in several data files from the proprietary laser-scanning package. These files included time; aircraft position in World Geodetic System 1984 (WGS84) latitude, longitude, and ellipsoidal elevation; aircraft attitude; raw laser range; pitch and angle mirror adjustments; laser nadir angle; vertical component of laser range; and the WGS84 Cartesian coordinates of the laser target. We wrote new scripts to extract and convert the high-precision geocentric coordinates of each ground surface reflection point from the original raw data files. After combining all data sections into a single file, the complete dataset was converted from the geocentric coordinates to WGS84 geodetic coordinates using GEOTRANS software (National Geospatial-Intelligence Agency). After the geocentric-to-geodetic conversion, the GEON Points2Grid Utility (Kim *et al.*, 2006) was used to convert the geodetic point cloud file into DEMs with grid densities of 0.5 m. The data were visualized as slope maps, aspect maps, and as shaded relief models illuminated and viewed from different angles.

Slip Measurement

We used LaDiCaoz, a MATLAB (see Data and Resources) cross-correlation code with a graphical user interface (GUI), and the measurement methods described by Zielke and Arrowsmith (2012) to make horizontal slip measurements using DEMs. To conduct our measurements, we clipped the entire Hector Mine LiDAR-based DEM data into 200 m × 200 m bins to meet the memory limits of MATLAB, generated hillshade maps, and then processed the DEM areas with the LaDiCaoz. Fault traces and upstream and downstream piercing lines were all defined in the GUI, and the parameters such as vertical shift, vertical stretch, and relative horizontal displacement were then optimized within the specified range. Next, linear features (e.g., the central line of the channel) that were assumed to be straight before the earthquake were regarded as references to measure the displacement. Two fault-parallel topographic profiles on either side of the fault were extracted and projected onto the fault plane. To measure the offset automatically and quantitatively, the extracted profiles were shifted and stretched incrementally relative to each other. Then the goodness of fit (GOF), which describes how well the two profiles matched each other, was calculated as the

inverse of the summed elevation difference between the two profiles.

In LaDiCaoz, the maximum GOF value corresponds to the optimal horizontal offset. Just as with field measurements, however, a reasonable range to cover all possible displacement should be estimated, because of the complexity of geomorphic features and nonuniqueness of measurement. After determination of GOF for each offset feature, hillshade maps were manually back slipped to visually determine acceptable upper and lower bounds of the measurement (Ⓔ the electronic supplement contains access information to view screen captures of the individual horizontal and vertical displacement measurements). The geomorphic complexity and estimated reliability are used as indicators of the feature with a quality rating of low, moderate-low, moderate, moderate-high, and high (Zielke and Arrowsmith, 2012; also Ⓔ see Tables S1 and S2). For completeness, in our LiDAR data analysis, we included all measurements, regardless of their quality ratings. Although these quality ratings are presented here, and some kind of relationship could be expected, we found no tendency for either high- or low-quality features to match the Treiman *et al.* (2002) field observations better or worse. This may be true because, as discussed later, there are only a few dozen collocated sites for which a detailed comparison is possible.

As part of this study, a MATLAB code was developed to obtain vertical offset measurements from the LiDAR data (Ⓔ for a complete list of the vertical offset data, see Table S2). After loading the DEM bins into the code, the trace of the fault and a local reference fault-perpendicular line were drawn manually on the computer screen. In this study, different distances (from 1 to 10 m) were tested, and we found that a 6 m wide swath, parallel to the fault, worked well for most cases. In rough, bouldery terrain, vertical topographic variations are averaged sufficiently by this approach. Thirteen topographic cross-fault profile slices (one on the reference fault-perpendicular line and six on either side of it), 0.5 m apart, were automatically generated parallel to and the same length as this reference line. The length of the reference fault-perpendicular line is site-specific because it had to be long enough to distinguish the hanging wall and the footwall, according to the local relief. To calculate the vertical offset at a given site, all cross-fault profiles were projected (stacked) onto the same vertical plane normal to the defined fault trace in an x–y coordinate system, with x representing the distance perpendicular to the fault and y representing the elevation. In the MATLAB GUI, boundaries of the fault scarp were determined manually by one person (Tao Chen). The elevation difference of the two endpoints was calculated automatically from where the positions of the boundaries crossed each cross-fault profile and then used as the approximation of vertical separation for this cross-fault profile.

The estimation of uncertainties of vertical offset did not use the same backslip method because we did not have a visual environment to check the restored original surface. Other studies (e.g., Thompson *et al.*, 2002) have used least-squares linear regressions of survey points along a terrace surface and across the fault to determine the mean and standard error of both the slope and the intercept of the lines representing the hanging wall and footwall. Thus, the measurement uncertainties of vertical offsets were calculated from the above mean and standard error. In our study, taking advantage of high-resolution LiDAR data, we automatically generated 13 crossline profiles at each location, as described above. The median value of the 13 vertical offsets was used as the vertical offset, and the standard deviation was also calculated as statistical dispersion of the measurement uncertainty. (Ⓔ The electronic supplement contains access information to view screen captures of the individual horizontal and vertical displacement measurements.)

Our code had significant limitations in measuring high-quality vertical offsets in areas with complicated pre-earthquake topography, or postearthquake colluvium deposition, which limited the total number of vertical offset measurements. Comparing with the field work, this method works well in places where we can assume that the geomorphic surface was originally planar before it was ruptured by the earthquake.

Results

In this study, we measured all displaced geomorphic features that were identifiable on the DEMs. Unlike the field investigations, we did not make any measurements from cultural features, such as vehicle tracks or bomb craters, because the LiDAR data contained a mix of pre-earthquake and postearthquake cultural features that could not be separated reliably. In addition, in this study we evaluate the advantages and disadvantages of using LiDAR data independently. Thus we used only LiDAR DEMs in this study, even though aerial photography was also available that could have potentially aided in finding more offset features and for comparisons. We obtained a total 255 horizontal and 85 vertical displacements using the LiDAR dataset (Ⓔ see Tables S1 and S2).

From the LiDAR DEMs, we found that the distribution of the dextral component of displacement along the entire fault trace is generally symmetric and has a roughly triangular shape with peak displacements of about 6–7 m located about 10 km southeast of the epicenter (Fig. 2a), in relatively good agreement with the field mapping data (Treiman *et al.*, 2002) (Ⓔ see Figure S1). We identified two data gap zones near the ends of the rupture where no LiDAR-based measurements could be made for at least 500 m along strike (see arrows in Fig. 2a). Sparse sampling density and difficulty with identifying surface features that could be used as piercing lines limited our ability to make any measurements in these gap zones. For the same two areas, field survey groups reported only two measurements near the 6 km location and no measurements near the 41 km location, which were all less than 1 m (Trieman *et al.*, 2002). This is roughly the critical threshold of high-quality measurements that can be made reliably with the available Hector Mine LiDAR data collected at that

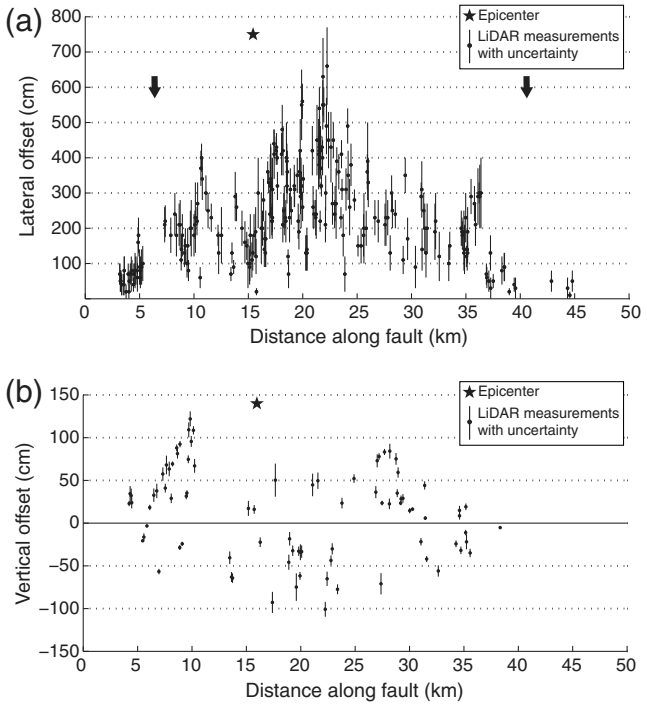

Figure 2. Distribution of (a) horizontal and (b) vertical offsets and measurement uncertainties plotted against distance along the surface rupture (0 km starts at the northernmost end). Distribution of horizontal slip along the fault is symmetric, with abrupt terminations of slip at the ends of the rupture. Sections of the fault where no measurements could be made with the LiDAR data are marked with black arrows. The sense of the vertical displacement component varies by fault segment. Both east-side down (+) and west-side down (−) measurements were made along the rupture. Lavic Lake fault dominantly has east-side down sense, whereas west-side down sense is more dominant near the epicenter where the fault bends westward.

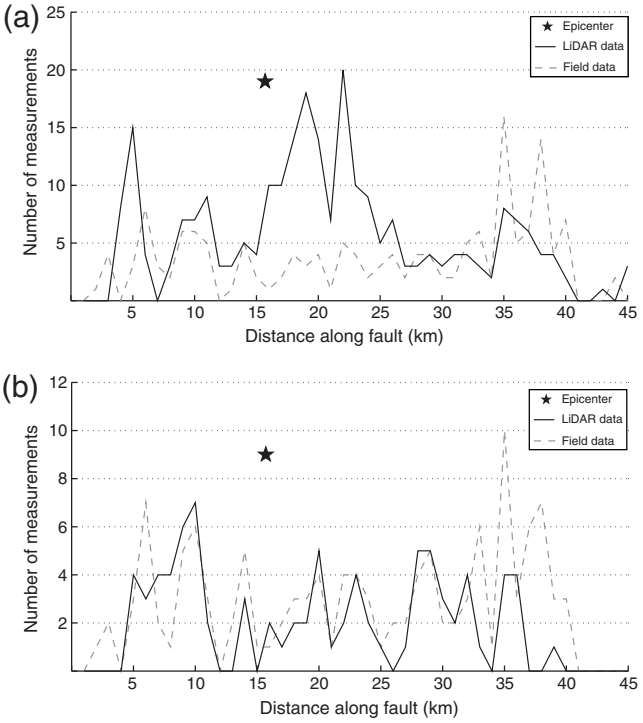

Figure 3. Comparison of (a) horizontal and (b) vertical total number of displacement measurements made at each kilometer in the field (dashed gray line) and by LiDAR data (black solid line) analysis.

time. For the vertical component of slip, the Hector Mine Earthquake Geologic Working Group surveyed 123 locations within the coverage of the LiDAR swath. The maximum vertical field offset was 1.40 ± 0.20 m (Treiman *et al.*, 2002). In contrast, we made 85 vertical offset measurements along the entire surface rupture using the LiDAR dataset (Fig. 2b).

We made more horizontal displacements per kilometer from the LiDAR data, compared to the number of displacements measured in the field, with the exception of the data gap zones near the ends of the rupture (Fig. 3a). Vertical measurement density was similar to that of the field measurements, except for the southernmost 10 km of the rupture (Fig. 3b). Generally, it is difficult to know the exact reasons why the densities of the horizontal measurements differ. The virtual field measurement on the computer screen emulates approaches conducted in the field work, while benefiting from convenient adjustment and unlimited repeat times. There may be several reasons for the difference. (1) As described by Oskin *et al.* (2007), the high-resolution DEM generated from the LiDAR data was easy to manipulate with Geographic Information System (GIS) software, and the measurable features were easy to visualize. (2) The natural environment (i.e., sun angle and accessibility of site) affects where and how often a displacement will be measured in the field. When time, access restrictions, or other logistical constraints limited the field investigation, measurements were generally made only in selected locations, with field investigators giving priority to displaced features where higher-quality (smaller uncertainty) measurements would be made. (3) Although the high-resolution aerial photographs acquired after an earthquake will allow more detailed examination of features, not all offset features will be clearly visible in such 2D images, depending on sun angle and ground surface contrast. The advantage of using a LiDAR DEM is that more offset features can be identified because of the 3D nature of the dataset, and all surface features where an offset can be identified may be readily measured.

The maximum right-lateral displacement measured from our LiDAR dataset is 6.60 ± 1.10 m. The field measurement located closest to this maximum value is only 4.85 ± 0.65 m (Fig. 4a); the highest field measurement, measured on offset vehicle tracks (5.25 ± 0.85 m), is 700 m to the north. Our measurement closest (less than 20 m) to the Treiman *et al.* (2002) field maximum is similar (5.40 ± 0.60 m; Fig. 4b). The second largest displacement measured from LiDAR data is 6.30 ± 1.10 m, and the nearest field measurement to that location (less than 100 m) is 4.70 ± 0.30 m (Fig. 4c). The maximum vertical displacement measured from LiDAR data

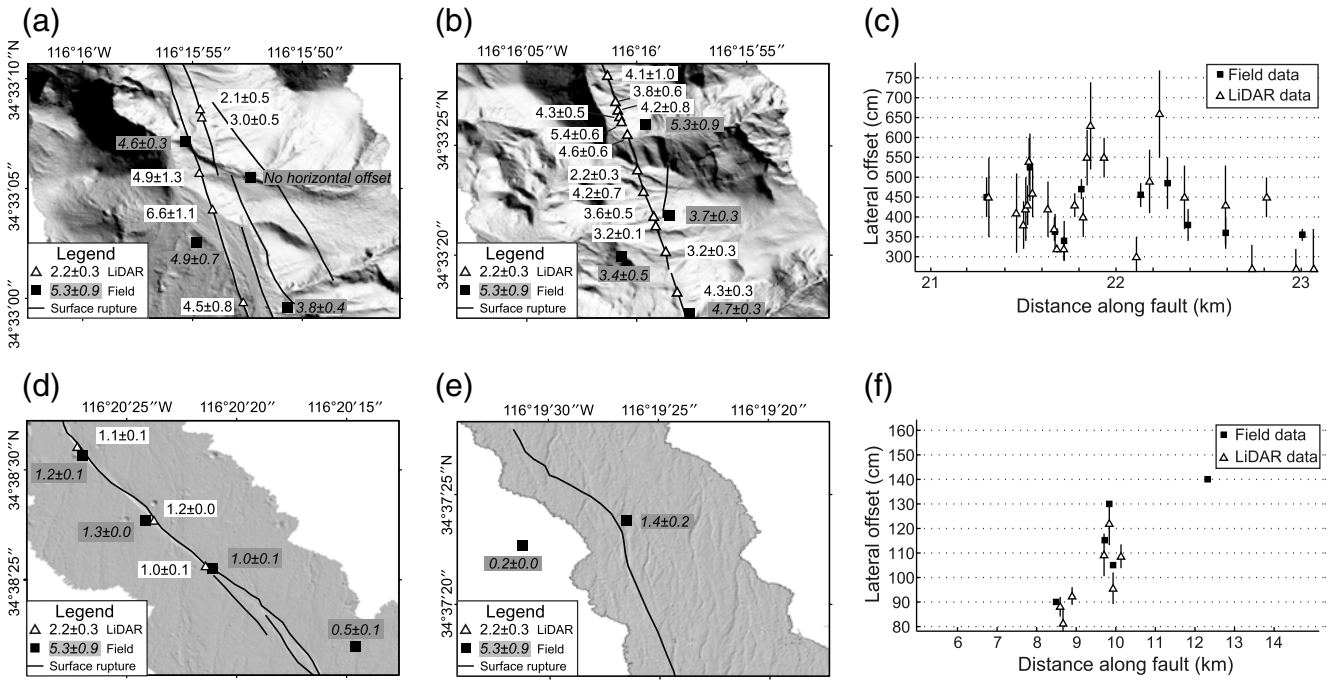

Figure 4. Comparison of right-lateral displacement measurements made in the field (black squares) and from LiDAR data (open triangles) at (a) the maximum LiDAR measurement site and (b) the maximum field measurement site. (c) The horizontal displacement measurement data presented in (a) and (b) are plotted along strike of the surface rupture of the fault. (d) Maximum vertical displacement measurements made using the LiDAR data compare well with the field data collected at the same stretch of the fault. (e) At or near the location where the maximum vertical displacement measurement was made in the field, no reliable vertical displacement measurements were made using the LiDAR data. (f) The vertical displacement data presented in (d) and (e) with respect to their locations are shown along the strike of the fault. Measurement locations are shown on the gray-scale shaded relief map derived from the LiDAR data.

is 1.22 ± 0.02 m, approximately 5 km northwest of the epicenter (Fig. 4d). There are no LiDAR measurements near the field maximum offset location (Fig. 4e,f), because the bar and swale topography of the coarse-grained alluvial fan deposits prevents a reliable measurement. These discrepancies illustrate one of the major limitations of the slip measurement study based only on remotely collected postearthquake topographic or imagery data.

For the average right-lateral displacement along the main break, Treiman *et al.* (2002) reported ~2.5 m. When the field data were used to study the shape of surface slip distributions, Wesnousky (2008) calculated the average displacement as the simplest curve fit and determined this value was ~1.6 m for the 1999 Hector Mine earthquake. Here, we present the average right-lateral displacement as normalized by distance along strike. We connect all the data points in Figure 2a to form a kinked curve, then integrate the area between the kinked curve and the x axis from the beginning to the end of the fault rupture, and finally divide this area by the total rupture length to obtain the normalized average right-lateral displacement. The error of this average displacement is estimated in the following steps: first each data point in Figure 2a is shifted up by its error, and the shifted points are connected as the second kinked curve. The area difference between the two kinked curves divided by the total length of the fault is considered as the error of the average displacement. This method yields an average displacement of 1.15 ± 0.15 m for the field dataset, and 1.72 ± 0.46 m for the LiDAR dataset. Because some of the measurements are likely minimum values, we also computed the average displacements of these datasets by integrating under an envelope defined by maximum data values (Wells and Coppersmith, 1994). Here, we define the envelope as the maximum displacement in each 1 km distance bin along the fault. The average displacement using the envelope method is 1.83 ± 0.21 m for the field data and 2.37 ± 0.50 m for the LiDAR data. In each case, the average displacement of the envelope is larger than the average displacement of the raw data, because some bins contained a relatively wide range (~3 m) of data values. This may be due to two effects: (1) some of the measurements were known to be only minimum values of offset (Treiman *et al.*, 2002) or contained measurement uncertainties (Gold *et al.*, 2013) and (2) surface displacement may have short wavelength variations over 10^1–10^2 m distance (e.g., Elliott *et al.*, 2009; Liu-Zeng *et al.*, 2010, Gold *et al.*, 2013).

The maximum vertical displacement value measured in this study is ~1.2 m (Fig. 2). The maximum vertical measurement did not occur at the same location of the maximum horizontal offset, but rather near the tail section of the rupture. The measurement density of the fieldwork and the LiDAR data look similar along most of the fault (Fig. 3b). Vertical displacements using LiDAR data also agree well with

the data from the field work. The sense of the vertical displacement has no consistent trend within the Bullion Mountains, but it is dominantly down to the east to the north and south of the Bullion Mountains (Fig. 2b).

Discussion

With the exception of the first pre- and postearthquake LiDAR differencing studies applied to the El Mayor–Cucapah earthquake (Oskin *et al.*, 2012) and the Darfield earthquake (Duffy *et al.*, 2013), a complete representation of 3D displacement along strike of a ruptured fault still remains a challenge. We tried to calculate both the horizontal and vertical offsets at the same locations, but due to various reasons, including rapid colluvium development along fault scarps immediately after the earthquake, and distributed deformation along wide (~10 m) fault zones, our dataset generally did not allow measurement of the full slip vector. It is generally difficult to measure vertical displacements in locations that are ideal for measuring horizontal displacements (e.g., linear features such as channels, channel margins, ridge lines) with or developed script. Hence, we could not achieve this goal of making collocated horizontal and vertical offset measurements. Given these challenges, we discuss the horizontal and vertical slip distributions separately.

Comparison of Horizontal and Vertical Displacements between LiDAR and Field Survey

Our horizontal measurements depended on the distribution of observable features across the fault trace. The horizontal offsets measured from both field and LiDAR will depend largely upon how these features are projected onto the fault plane and the nature of the features. For example, meandering stream channels, when projected across dozens-of-meters-wide deformation zones, may distort measurements from true values. The fault zone geometry and mechanics, such as multiple fault strands and block rotation, also could impact the reliability of the measurements. Second, postseismic deformation may need to be taken into account. Wilkinson *et al.* (2010) reported that in the months after the 2009 M_w 6.3 L'Aquila earthquake, the coseismic offsets were amplified up to 150%, as seen in repeating terrestrial laser scanner surveys.

It is important to note that the field data were collected starting immediately after the mainshock of the earthquake, LiDAR data were not collected until six months later. If postseismic deformation took place after the field survey and before the LiDAR flight, the LiDAR survey results might show higher offset values. This situation would be difficult to detect and eliminate based on only a single collection of postearthquake LiDAR data, but we can use GPS observations to help evaluate this. The GPS data collected after the Hector Mine earthquake indicated postseismic velocities consistent with continued right-lateral motion, with the maximum

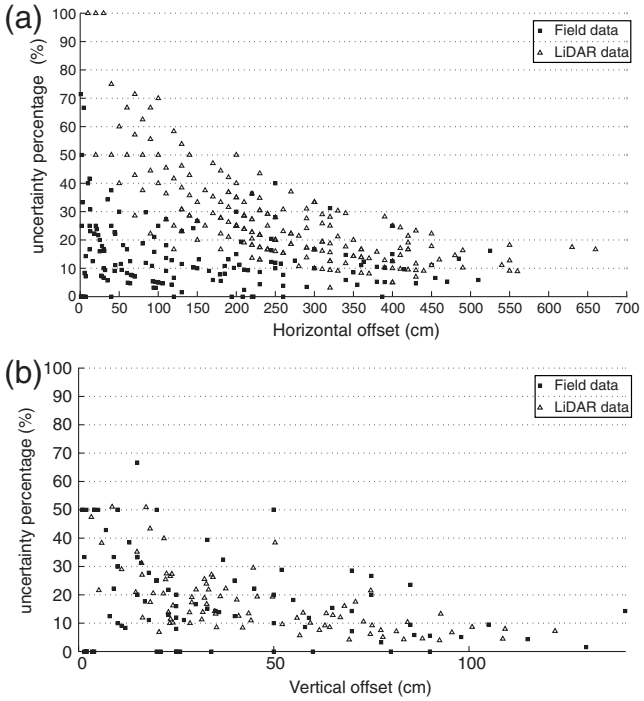

Figure 5. (a) Horizontal and (b) vertical measurement uncertainty percentages (uncertainty/displacement) are plotted against offset magnitudes for both field and LiDAR data. For horizontal offset measurements, whether they are made in the field or remotely from LiDAR data, measurement uncertainties decrease as the measurement magnitude increases.

rates decaying from ~10 cm/yr over the first 30 days to ~5 cm/yr over the following 130 days (Agnew *et al.*, 2002; Hudnut, King, *et al.*, 2002; Owen *et al.*, 2002). Thus, postearthquake deformation following the mainshock was negligible (less than 10 cm) and would not contribute much to the slip distribution. A detailed analysis of these offset measurements in the context of the coseismic surface rupture is outlined below.

First, we examine the uncertainties in the respective types of measurements. In general, LiDAR-based measurement uncertainties are higher than field measurement uncertainties (Fig. 5a). We showed this by comparing the offset magnitude with the uncertainty percentage calculated by dividing the measurement uncertainty by the actual measurement. To simplify the calculation, we used the mean value of the possibly upper and lower bounds of the measurement as the offset and made the uncertainties symmetric. When the lateral displacement magnitudes are less than 1 m, LiDAR-based measurements can have uncertainties up to 80% of the measurement value.

All measurements were done by one person (Tao Chen). Although all displacements were measured as carefully as possible, our uncertainties still do not account for individual bias. Several measurements with values less than 1 m and uncertainties near 100% of the measurement value were made but are eliminated from our analysis, as they were

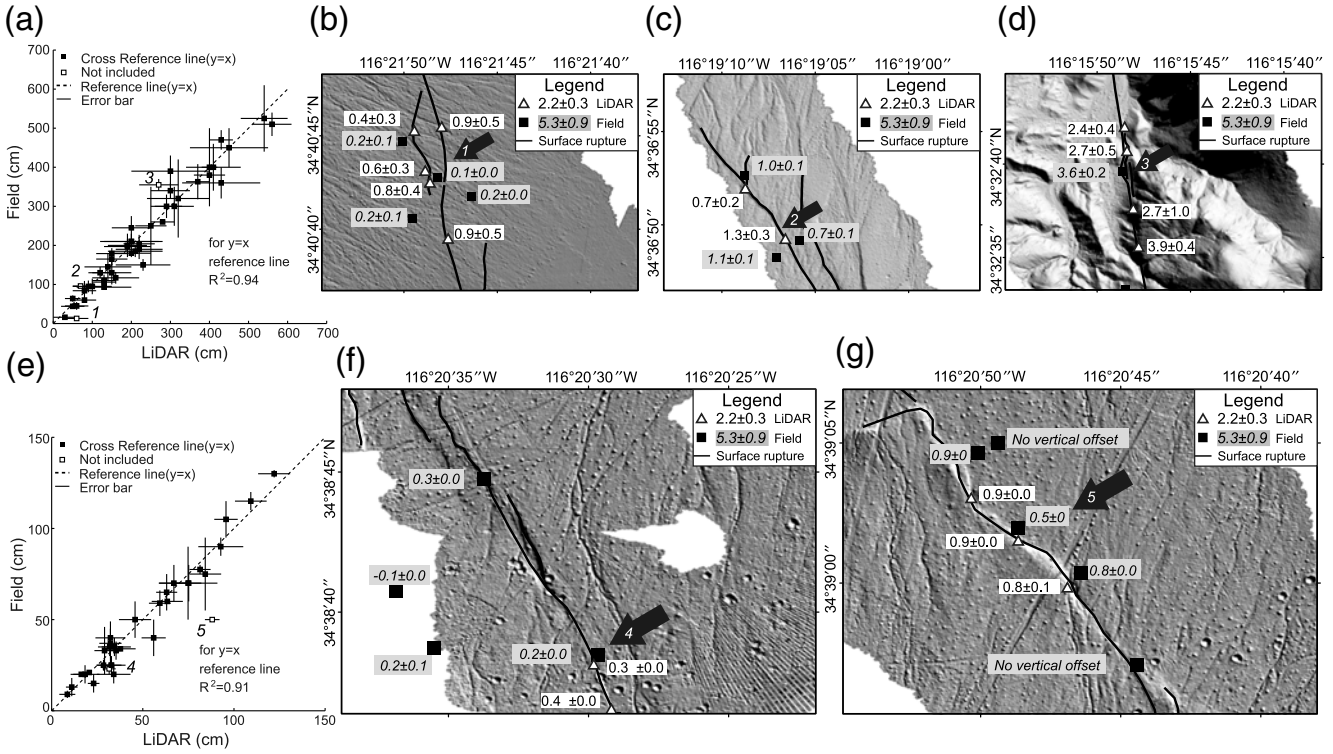

Figure 6. Comparison of field-based and LiDAR-based displacement measurements. (a) 44 collocated horizontal measurements. The detailed context of points marked 1, 2, 3 with open symbols in (a) are demonstrated by the gray-scale shaded relief maps (b–d); at these locations the field and LiDAR-based measurements do not agree. (e) 33 collocated vertical displacement measurements, (f, g) the contexts of vertical displacement measurements are indicated by points marked 4 and 5 in (e).

generally not reliable measurements. Once the lateral displacements reach or exceed 2.5 m, LiDAR-based measurement uncertainties shrink and become closer to field survey results. Conversely, uncertainties in the vertical components from LiDAR are found to be very comparable to the uncertainties in the field measurements of vertical offset, regardless of the displacement magnitude (Fig. 5b).

Of the field measurements, more than half (164/300) lie within the LiDAR-scanning coverage. We used a search buffer (20 m radius) to accommodate GPS positioning error and to identify locations where field and LiDAR measurements were possibly made on the same feature. This yielded 44 locations where measured offsets could be directly compared. Taking the measurement uncertainties into account, only 3 of these 44 locations could be regarded as outliers when the field and LiDAR measurements were assumed to be equal (Fig. 6a). LiDAR measurements at two of the three outliers (Fig. 6b,c) are of poor quality, indicating that even though reproducible measurements were made, features identified as piercing lines might not have preserved the evidence for the total displacement at that particular location. We are unable to further investigate the reasons behind the measurement discrepancies, as no descriptions or photos of these particular displaced features were included in Treiman *et al.* (2002). At the third location (Fig. 6d), both field investigations and our LiDAR analysis identified multiple parallel splays where the LiDAR measurement was made. It is possible that field measurements incorporated offsets from two or more fault strands, whereas the LiDAR measurement could only measure displacement across what is determined to be the primary fault line. We examined the coherence of measurements that should be equal and calculated R^2 (0.95) and the root mean square error (rmse; 32 cm); the former indicated a significant fit. Therefore, we conclude that displacements calculated from offset geomorphic features identified on LiDAR data are comparable to those made in the field, regardless of the magnitude of the displacement.

Using the similar method, we found that 33 field vertical measurement locations were within 20 m radius of LiDAR vertical measurement locations. The vertical measurements generated from two different methods were plotted and compared to a 1:1 reference line. The resulting R^2 value was 0.91 and the rmse was 9 cm (Fig. 6e). There were only two locations with poor quality. In one case, the measurement difference between field work and LiDAR was so small that it was within the measurement uncertainty (Fig. 6f). In the other case, it probably indicated that the field measurement was the minimum measurement at this location, relative to our LiDAR measurement (Fig. 6g).

We also compared unique lateral measurements (i.e., those not collocated within the 20 m search radius), 211 unique LiDAR-based and 120 unique field-based displacements. Each of the unique offset measurement sets represents a subset sampling of the whole offset distribution (Fig. 7a).

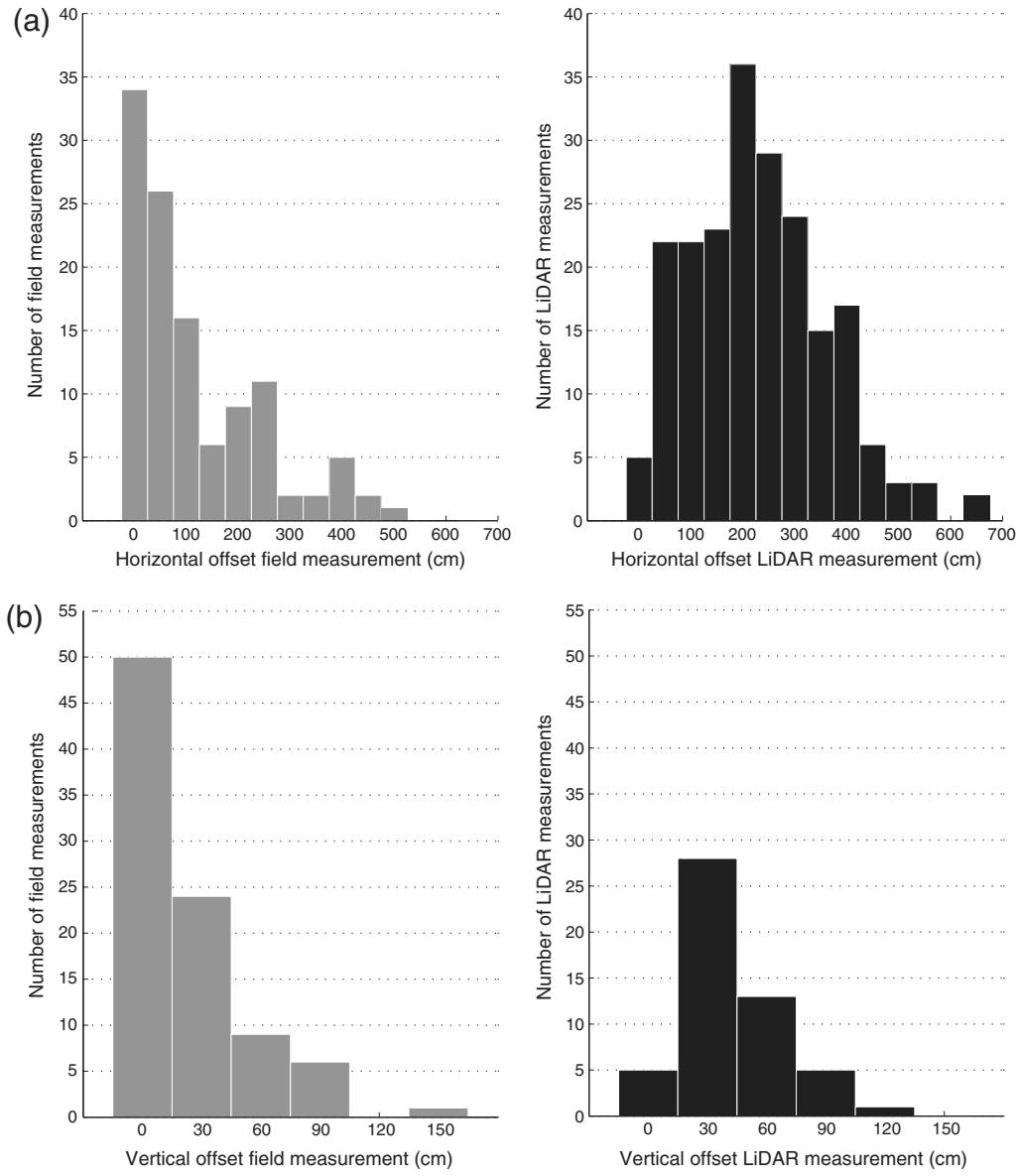

Figure 7. Histograms of unique (not collocated) (a) horizontal and (b) vertical displacement measurements made in the field or from LiDAR data, grouped based on 1 m (horizontal) and 30 cm (vertical) displacement bins. Over 50 unique horizontal measurements with values <1 m were made in the field. The 0.5 m LiDAR digital elevation model is not generally good enough to make such measurements unless the offset feature is very well developed.

The unique field offsets have an exponential distribution, whereas the unique LiDAR offsets have a normal distribution. The data show some skew, in that 30% of unique field offsets are less than 0.5 m and 54% of unique field offsets are less than 1 m; both percentages are higher than the LiDAR counterparts. This suggests the difficulty in identifying a geomorphic feature offset by less than 1 m with the available 0.5 m resolution DEMs, unless the geomorphic feature is exceptionally straight across the fault and at a high angle to the fault trace. For the vertical component, 90 unique field-based and 52 unique LiDAR-based displacements showed the same character described above We found that the limitation of vertical measurement based on 0.5 m resolution DEMs seemed to be 30 cm (Fig. 7b).

Influence of Rock Type

From north to south, there are three lithologies ruptured by the fault: basaltic lava flows, alluvium, and more silicic volcanic bedrock (lava and pyroclastic deposits; Dibblee, 1966, 1967a,b). For horizontal displacements, no LiDAR measurements and only one field measurement were made in the basaltic lava flow section. In the alluvium section, the numbers of offset measurements from LiDAR and field survey are very similar (151 versus 128), even though they are mostly in different locations (Fig. 8a). The percentages of collocated offsets (i.e., matched within the search radius) were also very close (21% versus 25%). In the volcanic bedrock section, the LiDAR dataset provided more measurements

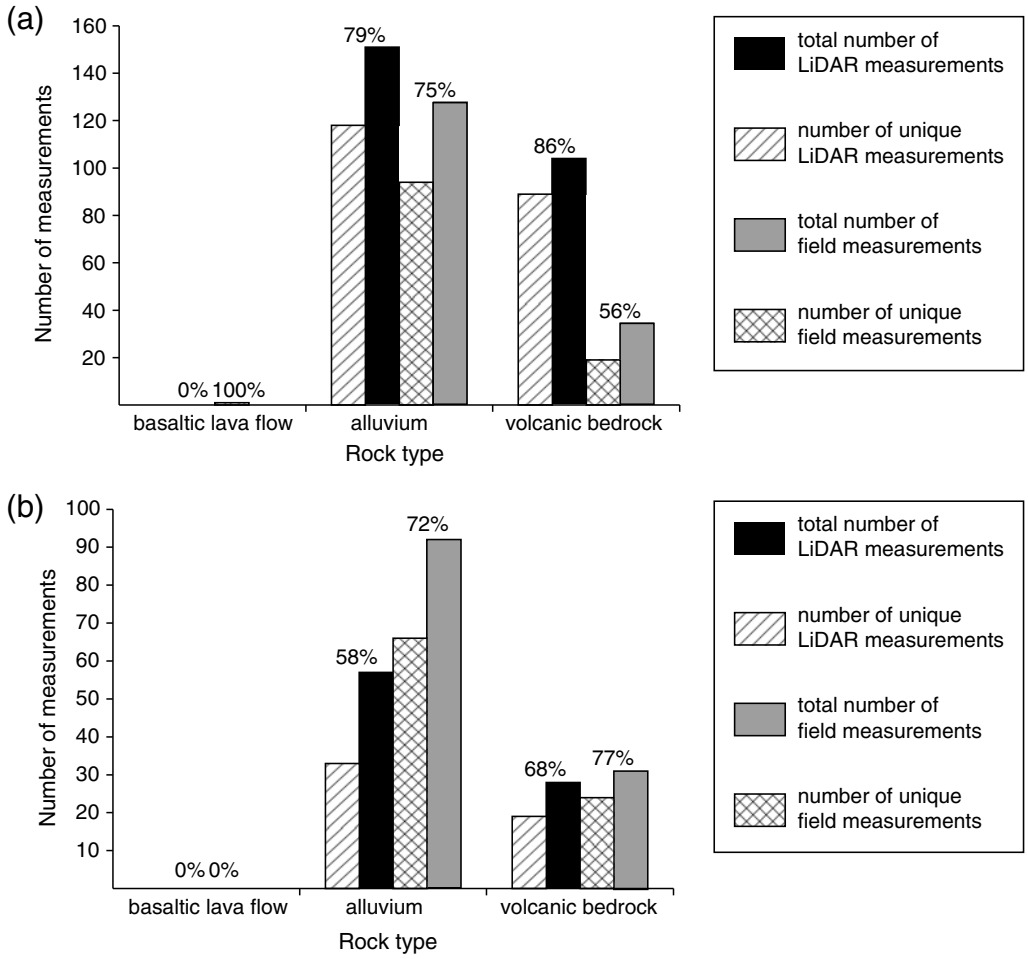

Figure 8. Analyses of the influence of rock type on locations where unique (a) horizontal and (b) vertical offset measurements were made in the field and with LiDAR data. No obvious effect of rock type on measurement locations is found.

than the field survey (104 versus 35; Fig. 8a). It is noticeable that 86% (89) of the LiDAR measurements made on volcanic bedrock are unique to this method. Only 33 of the field measurement locations within the volcanic bedrock were identified and measured with LiDAR data. The remaining two field measurements were outside of the LiDAR scanning coverage. We account that LiDAR data provided additional measurements because it is possible to visualize the data from different angles to better identify potential offset features. Comparing with the horizontal measurements, the vertical measurements were only measured in the alluvium section and the volcanic bedrock section (Fig. 8b). In the alluvium section, the number of vertical offsets measured from LiDAR is less than the number of field measurements (57 versus 93). In the volcanic bedrock section, the two numbers are very close (28 versus 30). This plot demonstrates that our vertical measurement method would work better in those locations where the original terrain was planar (Fig. 1c).

Along-Strike Variation of Horizontal Slip

Along-strike variability of slip within a short distance has been documented in detailed field investigations of numerous earthquakes, including Landers (McGill and Rubin, 1999), Hector Mine (Hudnut, Borsa, *et al.*, 2002; Treiman *et al.*, 2002), and Düzce (Rockwell *et al.*, 2002). Recent Co-registration of Optically Sensed Images and Correlation (COSI-Corr) analysis of the pre- and post-El Mayor–Cucapah earthquake using LiDAR data differencing also indicated that along-strike slip variations are likely real (Leprince *et al.*, 2011). This kind of variation might reflect actual lateral differences in the surface strain. However, there are several other potential factors (e.g., inelastic surface deformation, multiple distributed strands, nonplanar geometry, or measurement uncertainties) contributing to the slip variability, and differences in the surface setting (such as groundwater table, sedimentary consolidation, and stratal depths) would result in different relative contributions of the above factors (Shaw, 2011; Gold *et al.*, 2013). Hence which factor or factors are the most important varies with events, as well as with actual settings.

With high-resolution LiDAR data, we were able to study the entire Hector Mine surface rupture and critique the robustness of the conclusions about slip variations proposed after the initial analysis of the LiDAR data by Hudnut, Borsa, *et al.* (2002). For one of the best studied strike-slip surface-

rupturing earthquakes, the Hector Mine earthquake, the variations along strike over short distances reported by the Hector Mine Earthquake Geologic Working Group, and also documented in initial LiDAR analyses (Hudnut, Borsa, *et al.*, 2002), are similar in magnitude to those in the 1992 Landers earthquake (McGill and Rubin, 1999) and the 1999 Izmit earthquake (Rockwell *et al.*, 2002).

The measurements of surface slip along the Lavic and Bullion faults demonstrated slip variations at two scales, both of which could provide important insights into the 1999 rupture process. First, we identify a long wavelength (~15 km) variation in slip, corresponding to three distinct slip sections on the strike-slip faults along the whole rupture. The northernmost 15 km of the rupture typically had offsets of 0–3 m (Fig. 2). In the 10 km long middle section (between 15 and 25 km distance from the northern end of the rupture), almost all horizontal measurements are higher than 2 m and many are over 3 m, reaching values as high as 6.6 m. The southernmost half of the rupture (remaining 30 km) has horizontal displacements generally in the range of 0–3 m. Second, within these zones, shorter wavelength slip variations are seen. In particular, at a few locations within the middle section, several high-quality measurements with small uncertainties indicate large slip variations. Variation of offset as large as 3 m (consistent with the field measurements from 19 to 20 km) occurred within 10^1–10^2 m. Such short spatial scale slip variations are observed both south and north of the Bullion Mountains.

To faithfully represent measurement uncertainties and lack of data along certain sections of the faults, we quantitatively describe the along-strike variations using neighboring slip gradients (Elliott *et al.*, 2009). We first projected all of our measurement locations to a single reference fault line. We calculated the slip gradient between two neighboring measurement locations by dividing the difference between two displacements by the distance between those two locations. Starting from the north end, 230 slip gradient values were generated (Fig. 9a), excluding the sections of the fault where measurements were greater than 500 m apart. Because of these gaps between measurements, it is difficult to know whether the slip variation occurs over hundreds of meters or gradually over the entire distance, although we may find that InSAR datasets often show smooth gradients.

Regardless of the measurement uncertainties, the majority of the significant slip variations occur southeast of the epicenter, where slip was the highest (Fig. 9b). Analyses of seismic data suggest the Hector Mine earthquake initiated here at 5 ± 4 km depth on an unknown north-trending structure (Hauksson *et al.*, 2002) and continued on the Lavic Lake fault and Bullion fault zone. Deep, kilometer-scale structural complexity around the epicentral area of the Hector Mine earthquake thus seems a possible cause of the near-fault horizontal slip variations. These along-strike variations of slip may also be related to the fundamental physics of earthquake rupture, especially the asperities, which are strong fault patches that accumulate high preslip stress and lead to large coseismic slip, or the fault patches that resist coseismic slip

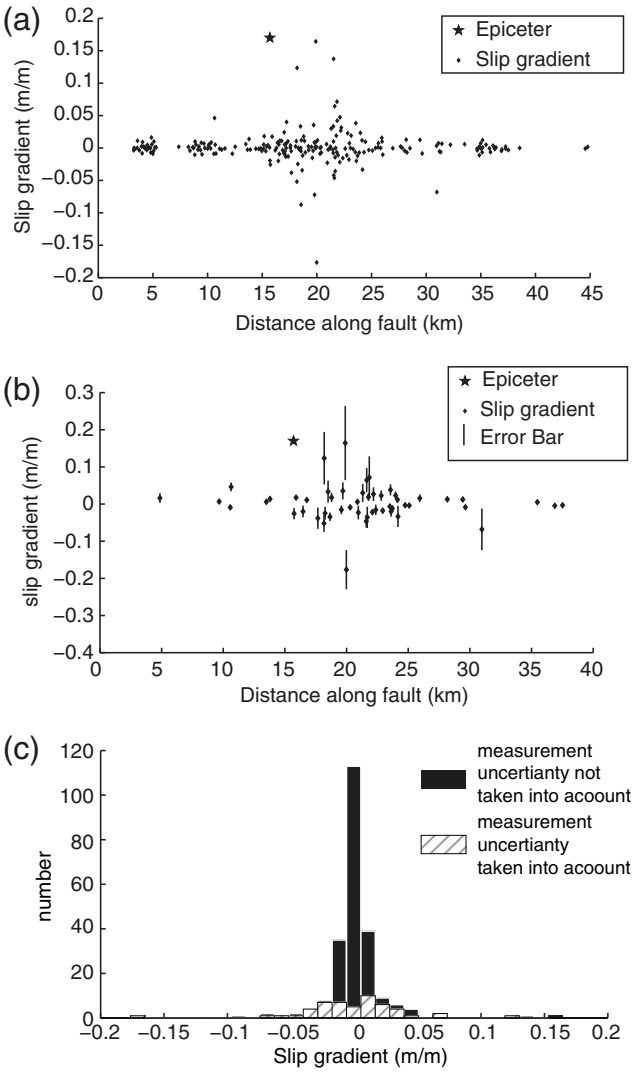

Figure 9. (a) Plot of slip gradient across the entire length of the surface rupture. The epicenter is marked with a black star. Note that maximum slip variations occur near where the largest horizontal slip was measured (Fig. 2). (b) Measurement uncertainties are considered and used to eliminate spans where the gradient could be zero due to measurement uncertainties. (c) Comparison of histograms when considering whether to include the slip measurement uncertainties.

and generate high postseismic stress (Kanamori and Stewart, 1978; Aki, 1984). A histogram of slip gradients followed a distribution very similar to a normal distribution with a mean value of 0 and a standard deviation of 0.0265 (Fig. 9c). This suggests that the variation of slip along the fault does not follow a systematic pattern and can be random.

If we exclude gradients that may be zero considering measurement uncertainties, we are left with ~50 of the original 230 slip gradient measurements (Fig. 9b). In other words, almost 80% of the gradients might be exaggerated by measurement uncertainties, which is compatible with results from airborne LiDAR differencing (Oskin *et al.*, 2012) and collected terrestrial laser scanning data (Gold *et al.*, 2013) after the El Mayor–Cucapah earthquake. The remaining gra-

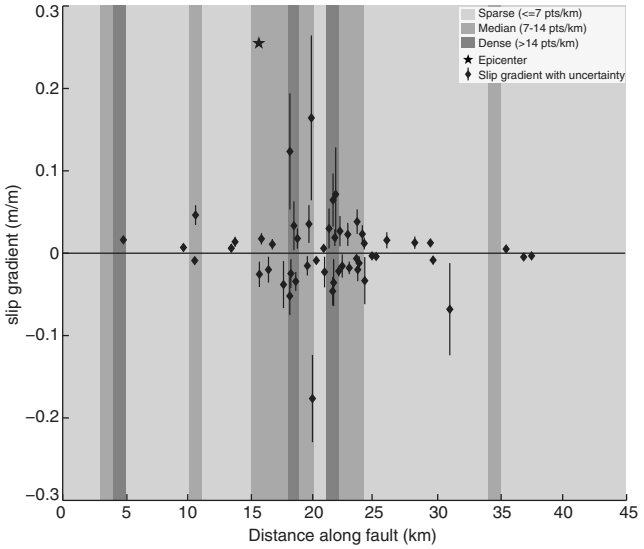

Figure 10. Investigation of the effect of measurement density on slip gradient. Total number of measurements made within each 1 km width of surface rupture are divided into three groups and shown in three different shades of gray. Lack of any obvious correlation suggests that measurement density introduce any slip gradient biases.

dients almost all lie in the epicentral area of the Hector Mine earthquake where the fault ruptured the Bullion Mountains. The histogram follows a similar pattern to the superposed plot, which represents the gradients including the measurement errors (Fig. 9c). Whether eliminating spans where the gradient could be zero due to measurement uncertainties or not, the variability of slip remains statistically random.

Because both field methods and our LiDAR analysis rely on identification of geomorphic features that are tectonically offset, spatial density of measurements can vary along strike. To investigate if sampling density has introduced any biases in interpreting slip gradient, we divided the entire rupture zone into 1 km wide bins, calculated the number of measurements made within each bin, and compared it with slip gradient calculations (Fig. 10). We separated the bins into three groups based on the number of horizontal measurements made within each bin. Our plot shows that while slip variations appear more often in areas with more measurements, bins with higher spatial density of measurements do not necessarily have higher magnitudes of slip variability. We therefore conclude that spatial density of horizontal displacements based on LiDAR data alone does not introduce significant bias in the slip gradients.

Although we excluded gradients that may be zero within error and analyzed the gradients with respect to measurement density, we still could not completely clarify the underlying factors that caused this kind of slip variation. To see through these noisy signals to find underlying trends, a 1 km wide moving window slide with 500 m long increment was applied along strike. Given constant strain, these slip distributions should increase linearly with separation. So we used a weighted least-square linear regression to fit all measurements in one window, and the weight is assigned as the reciprocal of the squared uncertainty (Gold *et al.*, 2013). We also calculate the unweighted mean square weighted deviation (MSWD), which should indicate how well the data fit the linear regression. In addition, the regression coefficient was regarded as the change in fault slip per unit distance along strike (along-fault strain). Hence most values of the strain were concentrated from 10^{-4} to 10^{-3}, with low MSWD (less than 1), except for the range from 10 to 25 km where the fault ruptured the Bullion Mountains, with high MSWD (higher than 3). As discussed above, deep structure or fundamental physics of earthquake rupture should play an important role in the slip variations near the epicentral region.

Conclusions

Results are presented for the first airborne LiDAR survey ever flown after a surface-rupturing earthquake for the purpose of assessing slip distribution. Detailed topographic images derived from the LiDAR data of the Hector Mine earthquake highlight the potential contribution of LiDAR surveying in both low-relief valley terrain and high-relief mountainous terrain.

We made 255 horizontal and 85 vertical displacement measurements using 0.5 m DEMs generated from the LiDAR dataset. The maximum horizontal offset value is 6.6 ± 1.1 m and is located approximately ~700 m south of the maximum horizontal offset observed during the field work. The average horizontal offset value from all LiDAR measurements, normalized by distance, is 1.72 ± 0.46 m, and the normalized average value calculated from a maximum-displacement envelope is 2.37 ± 0.50 m. The maximum vertical displacement measured from LiDAR data is ~1.2 m. No consistent trends are apparent in the sense of the vertical component, except in the northern mountainous section, which is dominated by east-side-down measurements.

Comparing with the field mapping dataset, LiDAR-based measurements (1) have larger measurement uncertainties, (2) have slightly higher values, (3) have difficulty resolving offsets < 1 m due to the DEM resolution, and (5) are spatially denser. The field investigation produced measurements of higher quality in alluvial deposits (e.g., vehicle tracks, offset rock, or pebble lineaments), which are not typically visible with 0.5 m resolution DEMs unless a piercing feature has a very large or clear offset. However, along the section of the fault that traverses exposed volcanic bedrock, LiDAR data provided additional measurements because it is possible to visualize the data from different angles to better identify possible offset features. The variation of slip along the fault does not demonstrate any systematic pattern, but we can see that the shortest scale has a large gradient nearest to the epicenter. Overall, the LiDAR measurements compared well, within stated errors, and also within a reasonable level of expected agreement with the field observations. The objective of attempting to attain a greater number of observations was achieved, but the LiDAR-based measurements had more uncertainty than did the field observations.

Similar to field studies that rely mainly on the presence of geomorphic features in making displacement measurements, slip variations based on the analysis of a postearthquake LiDAR data alone should be only accepted with caution. Multiple-event offsets, feature modification by off-fault deformation, and other sources of ambiguity can be associated with offset channels and other features. If earthquake surface rupture occurs in an area with dense cultural features (e.g., Darfield, New Zealand), postearthquake imagery alone has a chance to work well. Otherwise, we recommend differencing of LiDAR (i.e., Leprince *et al.*, 2011; Oskin *et al.*, 2012; Nissen *et al.*, 2014) and optical imagery (i.e., Binet and Bollinger, 2005; Ayoub *et al.*, 2009) data to better quantify the contributions of off-fault warping and displacements within distributed fault zones and provide more complete evidence for along-strike slip variations to better understand fault rupture processes associated with large magnitude strike-slip earthquakes.

Data and Resources

All data used in this article came from the published sources listed in the references. GEOTRANS (Geographic Translator) is an application program which allows one to easily convert geographic coordinates among a wide variety of coordinate systems, map projections, and datums. GEOTRANS 3.4 is now available, and can be downloaded from http://earth-info.nga.mil/GandG/geotrans/index.html (last accessed January 2015). MATLAB is the high-level language and interactive environment used to analyze and visualize in signal and image processing, communications, control systems, and computational finance. It can be downloaded from https://www.mathworks.com/programs/trials/trial_request.html?prodcode=ML&s_iid=main_trial_ML_nav (last accessed January 2015). Shuttle Radar Topography Mission data is available to be downloaded from http://eoweb.dlr.de (last accessed January 2015).

Acknowledgments

This research was supported by Public Service Funds for earthquake studies (201308012) and Fundamental Research Funds in the Institute of Geology (IGCEA1125). Tao Chen was sponsored as a visiting scholar to the U.S. Geological Survey (USGS) by the China Scholarship Council (Grant Number 2010419008). Work by D. Z. Zhang was supported, in part, by the Multi-Hazards Demonstration Project of the USGS. Jing Liu-Zeng and Kate Scharer helped us to improve the manuscript. We thank Katherine Kendrick for providing the database of field measurements from the original postearthquake observations of Treiman *et al.* (2002). We also thank an anonymous reviewer and Mike Oskin for their advice. Original LiDAR data acquisition was funded by the USGS and the Southern California Earthquake Center (SCEC). SCEC is funded by National Science Foundation Cooperative Agreement EAR-1033462 and USGS Cooperative Agreement G12AC20038. The SCEC contribution number for this article is 1973.

References

Agnew, D., S. Owen, Z.-K. Shen, G. Anderson, J. Svarc, H. Johnson, K. Austin, and R. Reilinger (2002). Coseismic displacements from the Hector Mine earthquake: Results from survey-mode GPS measurements, *Bull. Seismol. Soc. Am.* **92,** 1355–1364.

Aki, K. (1984). Asperities, barriers, characteristic earthquakes and strong motion prediction, *J. Geophys. Res.* **89,** 5867–5872.

Ayoub, F., S. Leprince, and J. P. Avouac (2009). Co-registration and correlation of aerial photographs for ground deformation measurements, *ISPRS J. Photogramm.* **64,** no. 6, 521–560.

Binet, R., and L. Bollinger (2005). Horizontal co-seismic deformation of the 2003 Bam (Iran) earthquake measured from SPOT-5 THR satellite imagery, *Geophys. Res. Lett.* **32,** no. 2, 1–9.

Bortugno, E. J. (1987). Calico, West Calico, Hidalgo and related faults, San Bernardino County, California, *Calif. Div. Mines Geol. Fault Evaluation Rept. FER-184*, 9 pp.

Cunningham, D., S. Grebby, K. Tansey, A. Gosar, and V. Kastelic (2006). Application of airborne LiDAR to mapping seismogenic faults in forested mountainous terrain, southeastern Alps, Slovenia, *Geophys. Res. Lett.* **33,** L20308, doi: 10.1029/2006GL027014.

Dibblee, T. W., Jr. (1966). Geologic map of the Lavic quadrangle, San Bernardino County, California, *U.S. Geol. Surv. Misc. Inv. Map I-472*, scale 1:48,000, 5 pp.

Dibblee, T. W., Jr. (1967a). Geologic map of the Deadman Lake quadrangle, San Bernardino County, California, *U.S. Geol. Surv., Misc. Inv. Map I-488*, scale 1:48,000, 5 pp.

Dibblee, T. W., Jr. (1967b). Geologic map of the Emerson Lake quadrangle, San Bernardino County, California, *U.S. Geol. Surv., Misc. Inv. Map I-490*, scale 1:48,000, 4 pp.

Duffy, B., M. Quigley, D. Barrell, R. Van Dissen, T. Stahl, S. Leprince, C. Mclnnes, and E. Bilderback (2013). Fault kinematics and surface deformation across a releasing bend during the 2010 M_w 7.1 Darfield, New Zealand, earthquake revealed by differential LiDAR and cadastral surveying, *Geol. Soc. Am. Bull.* **125,** nos. 3/4, 420–431.

Elliott, A. J., J. F. Dolan, and D. D. Oglesby (2009). Evidence from coseismic slip gradients for dynamic control on rupture propagation and arrest through stepovers, *J. Geophys. Res.* **114**, B2, 1–8.

Frankel, K. L., and J. F. Dolan (2007). Characterizing arid-region alluvial fan surface roughness with airborne laser swath mapping digital topographic data, *J. Geophys. Res.* **112**, F2, 1–14.

Gold, P., M. Oskin, A. Elliott, A. Hinojosa-Corona, M. H. Taylor, O. Kreylos, and E. Cowgill (2013). Coseismic slip variation assessed from terrestrial LiDAR scans of the El Mayor–Cucapah surface rupture, *Earth Planet Sci. Lett.* **366,** 151–162.

Haeussler, P. J., D. P. Schwartz, T. E. Dawson, H. D. Stenner, J. J. Lienkaemper, B. Sherrod, F. R. Cinti, P. Montone, P. A. Craw, A. J. Crone, and S. F. Personius (2004). Surface rupture and slip distribution of the Denali and Totschunda faults in the 3 November 2002 **M** 7.9 earthquake, Alaska, *Bull. Seismol. Soc. Am.* **94,** no. 6, 23–52.

Hart, E. W. (1987). Pisgah, Bullion and related faults, San Bernardino County, California, *Calif. Div. Mines Geol., Fault Evaluation Rept.FER-188*, 4 pp.

Haugerud, R., D. J. Harding, S. Y. Johnson, J. L. Harless, C. S. Weaver, and B. L. Sherrod (2003). High-resolution LiDAR topography of the Puget lowland, Washington–A bonanza for earth science, *GSA Today* **13,** 4–10.

Hauksson, E., L. M. Jones, and K. Hutton (2002). The 1999 M_w 7.1 Hector Mine, California, earthquake sequence: Complex conjugate strike-slip faulting, *Bull. Seismol. Soc. Am.* **92,** no. 4, 1154–1170.

Hector Mine Earthquake Geologic Working Group (1999). Surface rupture, slip distribution, and other geologic observations associated with the **M** 7.1 Hector Mine earthquake of 16 October 1999, *AGU Fall Meeting Program*, San Francisco, California, 13–17 December 1999, 11 pp.

Hudnut, K. W., A. Borsa, C. Glennie, and J. B. Minster (2002). High-resolution topography along surface rupture of the 16 October 1999 Hector Mine, California, earthquake (M_w 7. 1) from airborne laser swath mapping, *Bull. Seismol. Soc. Am.* **92,** 1570–1576.

Hudnut, K. W., N. E. King, J. G. Galetzka, K. F. Stark, J. A. Behr, A. Aspiotes, S. van Wyk, R. Moffitt, S. Dockter, and F. Wyatt (2002). Continuous GPS observations of postseismic deformation following the 16 October 1999 Hector Mine, California, earthquake, *Bull. Seismol. Soc. Am.* **92,** 1403–1422.

Kanamori, H., and G. S. Stewart (1978). Seismological aspects of Guatemala earthquake of February 4, 1976, *J. Geophys. Res.* **83,** 3427–3434.

Kim, H., J. R. Arrowsmith, C. J. Crosby, E. Jaeger-Frank, V. Nandigam, A. Memon, J. Conner, S. B. Badden, and C. Baru (2006). An efficient implementation of a local binning algorithm for digital elevation model generation of LiDAR/ALSM dataset (abstract G53C-0921), *Eos Trans. AGU* **87,** no. 52 (Fall Meet. Suppl.), G53C-0921.

Klinger, Y., X. Xu, P. Tapponnier, J. Van der Woerd, C. Lasserre, and G. King (2005). High-resolution satellite imagery mapping of the surface rupture and slip distribution of the M_w 7.8, 14 November 2001 Kokoxili earthquake, Kunlun fault, northern Tibet, China, *Bull. Seismol. Soc. Am.* **95,** 1970–1987.

Leprince, S., K. W. Hudnut, S. O. Akciz, A. Hinojosa-Corona, and J. M. Fletcher (2011). Surface rupture and slip variation induced by the 2010 El Mayor–Cucapah earthquake, Baja California, quantified using COSI-Corr analysis on pre- and postearthquake LiDAR acquisitions (abstract EP41A-0596), *Eos Trans. AGU* **92,** no. 52 (Fall Meet. Suppl.), EP41A-0596.

Li, D. (2009). Remote sensing in the Wenchuan earthquake, *Photogramm. Eng. Rem. S.* **75,** no. 5, 507–509.

Liu-Zeng, J., L. Wen, J. Sun, Z. Zhang, G. Hu, X. Xing, L. Zeng, and Q. Xu (2010). Surficial slip and rupture geometry on the Beichuan fault near Hongkou during the M_w 7.9 Wenchuan earthquake, China, *Bull. Seismol. Soc. Am.* **100,** 2615–2650.

Liu-Zeng, J., Z. Zhang, L. Wen, P. Tapponnier, J. Sun, X. Xing, G. Hu, Q. Xu, L. Zeng, L. Ding, C. Ji, K. Hudnut, and J. van der Woerd (2009). Co-seismic ruptures of the 12 May, 2008, M_w 8.0 Wenchuan earthquake, Sichuan: EW crustal shortening on oblique, parallel thrusts along the eastern edge of Tibet, *Earth Planet. Sci. Lett.* **286,** 355–370.

McGill, S. F., and C. M. Rubin (1999). Surficial slip distribution on the central Emerson fault during the 28 June 1992 Landers earthquake, California, *J. Geophys. Res.* **104,** 4811–4833.

Nissen, E., T. Maruyama, J. R. Arrowsmith, J. Elliott, A. Krishnan, M. Oskin, and S. Saripalli (2014). Coseismic fault zone deformation revealed with differential LiDAR: Examples from Japanese $M_w \sim 7$ intraplate earthquakes, *Earth Planet. Sci. Lett.* **405,** 244–256.

Oskin, M. E., J. R. Arrowsmith, A. H. Corona, A. J. Elliott, J. M. Fletcher, E. J. Fielding, P. O. Gold, J. J. G. Garcia, K. W. Hudnut, J. Liu-Zeng, and O. J. Teran (2012). Near-field deformation from the El Mayor–Cucapah earthquake revealed by differential LiDAR, *Science* **335,** 702–705.

Oskin, M. E., K. Le, and M. D. Strane (2007). Quantifying fault-zone activity in arid environments with high-resolution topography, *Geophys. Res. Lett.* **34,** no. 23, L23S05, doi: 10.1029/2007GL031295.

Owen, S., G. Anderson, D. C. Agnew, H. Johnson, K. Hurst, K. R. Reilinger, Z.-K. Shen, and J. Svarc (2002). Early postseismic deformation from the 16 October 1999 M_w 7.1 Hector Mine, California, earthquake as measured by survey-mode GPS, *Bull. Seismol. Soc. Am.* **92,** no. 1, 1423–1432.

Prentice, C. S., C. J. Crosby, D. J. Harding, R. A. Haugerud, D. J. Merritts, T. Gardner, R. D. Koehler, and J. N. Baldwin (2003). Northern California LiDAR data: A tool for mapping the San Andreas fault and Pleistocene marine terraces in heavily vegetated terrain (abstract G12A-06), *Eos Trans. AGU* **84,** no. 46 (Fall Meet. Suppl.), G12A-06.

Prentice, C. S., P. Mann, A. J. Crone, R. D. Gold, K. W. Hudnut, R. W. Briggs, R. D. Koehler, and P. Jean (2010). Tectonic geomorphology and seismic hazard of the Enriquillo–Plantain Garden fault in Haiti, *Nat. Geosci.* **3,** 789–793.

Quigley, M., R. Van Dissen, N. Litchfield, P. Villamor, B. Duffy, D. Barrell, K. Furlong, T. Stahl, E. Bilderback, and D. Noble (2012). Surface rupture during the 2010 M_w 7.1 Darfield (Canterbury, New Zealand) earthquake: Implications for fault rupture dynamics and seismic-hazard analysis, *Geology* **40,** no. 1, 55–58.

Rockwell, T. K., S. Lindvall, T. Dawson, R. Langridge, W. Lettis, and Y. Klinger (2002). Lateral offsets on surveyed cultural features resulting from the 1999 Izmit and Duzce earthquakes, Turkey, *Bull. Seism. Soc. Am.* **92,** no. 1, 79–94.

Rymer, M. J., G. G. Seitz, K. D. Weaver, A. Orgil, G. Faneros, J. C. Hamilton, and C. Goetz (2002). Geologic and paleoseismic study of the Lavic Lake fault at Lavic Lake playa, Mojave Desert, southern California, *Bull. Seismol. Soc. Am.* **92,** 1577–1591.

Salisbury, J. B., T. K. Rockwell, T. J. Middleton, and K. W. Hudnut (2012). LiDAR and field observations of slip distribution for the most recent surface ruptures along the central San Jacinto fault, *Bull. Seismol. Soc. Am.* **102,** 598–619.

Sauber, J., W. Thatcher, S. C. Solomon, and M. Lisowski (1994). Geodetic slip rate for the eastern California shear zone and the recurrence time of Mojave Desert earthquakes, *Nature* **367,** 264–266.

Shaw, B. E. (2011). Surface-slip gradients of large earthquakes, *Bull. Seismol. Soc. Am.* **101,** no. 2, 792–804.

Thompson, S. C., R. J. Weldon, C. M. Rubin, K. Abdrakhmatov, P. Molnar, and G. W. Berger (2002). Late Quaternary slip rates across the central Tien Shan, Kyrgyzstan, central Asia, *J. Geophys. Res.* **107,** no. B9, 2203, doi: 10.1029/2001JB000596.

Treiman, J. A., K. J. Kendrick, W. A. Bryant, T. K. Rockwell, and S. F. McGill (2002). Primary surface rupture associated with the M_w 7.1 16 October 1999 Hector Mine earthquake, San Bernardino County, California, *Bull. Seismol. Soc. Am.* **92,** 1171–1191.

Wells, D. L., and K. J. Coppersmith (1994). New empirical relationships among magnitude, rupture length, rupture width, rupture area, and surface displacement, *Bull. Seismol. Soc. Am.* **84,** 974–1002.

Wesnousky, S. G. (2008). Displacement and geometrical characteristics of earthquake surface ruptures: Issues and implications for seismic hazard analysis and the earthquake rupture process, *Bull. Seismol. Soc. Am.* **98,** 1609–1632.

Wilkinson, M., K. J. W. McCaffrey, G. Roberts, P. A. Cowie, R. J. Phillips, A. M. Michetti, E. Vittori, L. Guerrieri, A. M. Blumetti, A. Bubeck, *et al.* (2010). Partitioned postseismic deformation associated with the 2009 M_w 6.3 L'Aquila earthquake surface rupture measured using a terrestrial laser scanner, *Geophys. Res. Lett.* **37,** L10309, doi: 10.1029/2010GL043099.

Zielke, O., and J. R. Arrowsmith (2012). LaDicaoz and LiDARIMAGER-MATLAB GUIs for LiDAR data handling and lateral displacement measurement, *Geosphere* **8,** 206–221.

Zielke, O., J. R. Arrowmith, L. Grant Ludwig, and S. O. Akciz (2010). Slip in the 1857 and earlier large earthquakes along the Carrizo Plain, San Andreas fault, *Science* **327,** 1119–1122.

State Key Laboratory of Earthquake Dynamics
Institute of Geology, China Earthquake Administration
Yard No. 1, Hua Yan Li
Chaoyang District, Beijing 100029 China
chent@cea.gov.cn
(T.C.)

Department of Earth Planetary and Space Sciences
University of California
405 Hilgard Avenue
Los Angeles, California 90095
(S.O.A.)

United States Geological Survey
525 South Wilson Avenue
Pasadena, California 91106
(K.W.H.)

Seismological Laboratory
Department of Geological and Planetary Sciences
California Institute of Technology
1200 E California Boulevard
Pasadena, California 91125
(D.Z.Z., J.M.S.)

Manuscript received 2 May 2013;
Published Online 3 February 2015